Reviewers' Comments to Authors:

Reviewer #1 :

General Comments:

The subject of this manuscript is essentially the Antarctic cell of the Meridional Overturning Circulation (MOC) which studied on the basis of Glorys12 reanalysis using Constituent-oriented Age and Residence time Theory. The aim of the work is to establish the asymmetry of the return flow coming from the Pacific, Indian and Atlantic oceans within this cell to the Southern Ocean. The idea behind the study seems quite reasonable. However, it lacks quantitative results that would allow us to verify both the quality of the calculations performed and the adequacy of the tools and data used. The tools used in the task are not fully described. The provided illustrations contain obvious errors. The manuscript requires **major revision**.

Response: We thank the reviewer for the careful evaluation and constructive comments. We have added a regional decomposition of concentration-weighted upward transport, assessed inversions and surface intersections in the three-dimensional neutral-density field, and compared the hydrographic structure with WOA23. We have also clarified the tracer initial and source conditions, the time basis of the diagnostics, and the transport definitions, and corrected the geographic and physical descriptions identified below.

Specific Comments

1. The authors attempt to confirm that the primary upward transport within this cell, from the lower to the upper branch, is concentrated directly in the Southern Ocean. In this situation, the authors can provide estimates of vertical cross-isopycnal transport specifically for the Southern Ocean, defining its northern boundary, for example, at 40°S, as well as for each of the remaining parts of the three oceans separately. The resulting estimates can be compared with existing estimates of the Antarctic cell transport. Such a comparison can serve as a criterion for the quality of the calculations performed and the adequacy of the tools used to solve the problem, estimates for which are lacking in the current version of the manuscript. In this regard, it would be appropriate to include in the Introduction the intensities of both the Antarctic MOC cell and the Atlantic MOC cell, associated with deep water lowering in the North Atlantic. Here are a few references:

Atlantic cell (14-18 Sv):

1. Inverse box model of the World Ocean (A. Ganachaud // J. Geophys. Res., 2003, 108(C7), 3213. DOI: 0.1029/2002JC001565)

2. The transport balance across the Subantarctic Front in the Southern Ocean (!) between three components: the Ekman transport in the surface layer of the ocean, the eddy transport across the front, and also the transverse transport to the front by

geostrophic currents below the crests of the ridges crossing the Antarctic Circumpolar Current (M.N. Koshlyakov, R.Yu. Tarakanov // Oceanology, 2011, 51(5), 721. DOI: 10.1134/S0001437011050110).

3. Direct mathematical modeling of ocean water circulation (R. Marsh, A.J.G. Nurser, A.P. Megann, A.L. New // J. Phys. Oceanogr., 2000, 30(5), 1013. DOI: 10.1175/1520-0485(2000)030<1013:WMTITS>2.0.CO;2).

4. Generalization of hydrographic measurement data (W.J. Schmitz, Jr. // On the World Ocean Circulation: Volume II, The Pacific and Indian Oceans. A Global Update, Woods Hole Oceanog. Inst. Tech. Rept., WHOI–96–08, 1996, 237 pp).

Antarctic cell (transport 15-20 Sv based on the balance of various tracers, i.e. freons, radiocarbon, quasi-conservative phosphate complex, etc., directly in the Southern Ocean, which gives the most reliable estimates):

1. W.S. Broecker, S.L. Peacock, S. Walker, R. Weiss, E. Fahrbach, M. Schroeder, U. Mikolajevich, E. Heinze, R. Key, T.-H. Peng, S. Rubin // J. Geophys. Res., 1998, 103(C8), 15833. DOI: 10.1029/98JC00248.

2. S. Peacock, M. Visbeck, W.S. Broecker In: Inverse Methods in Global Biogeochemical Cycles, Geophys. Monogr. Ser., 114, Eds P. Kasibhatla, M. Heimann, P. Rayner et al.,USA, D.C., Washington, AGU Publ., 2000, pp. 185–195. DOI: 10.1029/GM114p0185.

3. A.H. Orsi, W.M. Smethie, J.L. Bullister // J. Geophys. Res., 2002, 107(C8). DOI: 10.1029/2001JC000976. Other methods yield a much wider range of transports for the Antarctic cell. The list of papers providing transport estimates for both cells is much longer. If necessary, more recent studies can be easily found using the list provided.

Response: We thank the reviewer for this suggestion. Following the proposed 40°S division, we have added a regional decomposition of upward concentration-weighted diapycnal transport for the Southern Ocean and the three basin interiors (Supplementary Fig. S5). We have also added published estimates of both overturning cells and the upward return branch to the Introduction.

We carefully examined the transport estimates and references suggested by the reviewer. These studies primarily constrain the formation and deep-ocean input side of the overturning circulation. In the North Atlantic, inverse and tracer-based estimates place North Atlantic Deep Water formation and export at approximately 14–18 Sv. In the Southern Ocean, tracer-budget estimates indicate approximately 14–21 Sv of Antarctic water input to the deep ocean, depending on the water masses and entrainment included in the calculation (Broecker et al., 1998; Peacock et al., 2000; Orsi et al., 2002). For example, Orsi et al. (2002) estimated approximately 13.7 Sv of Antarctic near-surface-water input, increasing to about 21 Sv when the entrained subsurface component is included.

Because the present study focuses on the complementary upward return of bottom water, we have also added quantitative estimates from previous studies of the return branch. Mixing-based calculations indicate approximately 6 Sv of bottom-water upwelling north of 30°S associated with locally dissipating tidal mixing (De Lavergne et al., 2016), while Lagrangian analyses estimate approximately 13–21 Sv of deep-water transport from 30°S to the Southern Ocean mixed layer (Tamsitt et al., 2017, 2018). These estimates are not strictly equivalent because they refer to different water masses, spatial boundaries, and transport definitions. We therefore use them to provide quantitative context for the different components of overturning transport rather than as one-to-one equivalents of the concentration-weighted upward flux diagnosed here.

Following this suggestion, we added the following text to the Introduction section of the revised manuscript:

> *"Quantitative estimates provide complementary constraints on the formation and return branches of the overturning circulation. In the North Atlantic, inverse and tracer-based estimates place the formation and southward export of North Atlantic Deep Water (NADW) at approximately 14–18 Sv (Ganachaud, 2003; Broecker et al., 1998). In the Southern Ocean, tracer budgets indicate a comparable input of Antarctic waters to the deep ocean, with estimates of approximately 14–21 Sv depending on the water masses and entrainment included in the calculation (Broecker et al., 1998; Peacock et al., 2000; Orsi et al., 2002). Estimates of the upward return are also of order 10 Sv but depend strongly on the process and diagnostic considered. Mixing-based calculations indicate several Sverdrups of AABW upwelling in the abyssal ocean, with approximately 6 Sv attributed to locally dissipating tidal mixing north of 30°S (De Lavergne et al., 2016), while Lagrangian analyses estimate approximately 13–21 Sv of deep-water transport from 30°S to the Southern Ocean mixed layer (Tamsitt et al., 2017, 2018). These estimates refer to different water masses, spatial boundaries, and transport definitions, but together provide quantitative context for the downward formation and upward return branches of the global overturning circulation."*

We also revised the beginning of the following paragraph to connect these transport estimates with the regional mechanisms discussed subsequently:

> *"Beyond these basin-scale transport estimates, observational and modeling studies have constrained the regional mechanisms that organize abyssal return."*

At the same time, we fully agree with the reviewer that the present manuscript would benefit from a quantitative regional decomposition of the upward bottom-water transport. Following this suggestion, we therefore integrated the upward concentration-weighted diapycnal flux separately over the Southern Ocean south of 40°S and over the Atlantic, Pacific, and Indian Oceans north of 40°S. The results are now shown in a new

Supplementary Figure S5, and the original Supplementary Figure S5 has been renumbered as Figure S6.

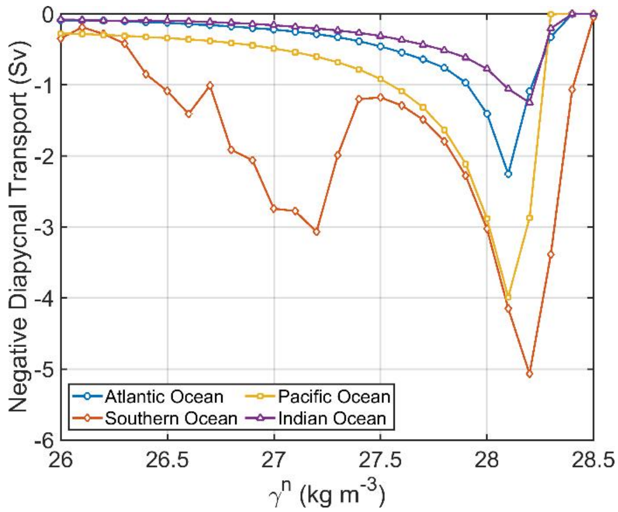

"Figure S5. Regional upward concentration-weighted diapycnal transport (Sv) across neutral-density surfaces spaced at intervals of $0.1\ kg\ m^{-3}$ *for the Southern Ocean south of 40° S and the Atlantic, Pacific, and Indian Oceans north of 40° S. Negative values denote transport toward lighter density classes, following the sign convention in Sect. 2.4 of the main text. Each curve shows the density dependence of one regional contribution. Contributions across a common surface are compared at the same neutral density."*

As shown in Supplementary Fig. S5, the Southern Ocean provides the largest individual regional contribution over most of the deep and abyssal density range, reaching approximately 5 Sv near $\gamma^n \approx 28.2$ kg m^{-3}. The peak magnitudes on the separate Pacific, Atlantic, and Indian curves are approximately 4.0, 2.3, and 1.3 Sv, respectively. Regional contributions are compared at the same density; the separate curve maxima are not summed. These are upward concentration-weighted contributions, whereas the cited overturning estimates use different source definitions, boundaries, and net or gross transport measures. Their comparison provides quantitative context for the return pathways, while Fig. S5 directly quantifies the regional partition within the present diagnostic.

The corresponding paragraph in Sect. 3.2 now reads:

"To quantify the regional distribution of upward bottom-water transport, we further integrated the upward concentration-weighted diapycnal flux separately over the Southern Ocean south of 40°S and over the Atlantic, Pacific, and Indian Oceans north of 40°S (Supplementary Fig. S5). The Southern Ocean exhibits the largest individual regional contribution to upward concentration-weighted transport over most of the abyssal-to-deep density range, with a peak magnitude of about 5 Sv near $\gamma^n \approx 28.2$ *kg m*$^{-3}$*. The corresponding peak values of the separate regional curves are*

approximately 4.0 Sv in the Pacific, 2.3 Sv in the Atlantic, and 1.3 Sv in the Indian Ocean. This regional partition supports the Southern Ocean as the leading regional gateway for upward transformation of bottom-water influence in the diagnosed fields. These regional maxima characterize separate density-dependent curves; contributions to transport across a common surface must be compared at the same density."

2. The main problem of this manuscript becomes apparent when examining Figure S3 in the Supplement. In particular, the presence of neutral density inversions raises questions. These inversions may be related to the zonal averaging that these figures correspond to. However, the entire reanalysis dataset may contain a large number of such inversions, which calls into question the appropriateness of using this dataset to address the problem addressed by the authors. The dataset should be checked for the presence of such inversions. The topography of surface 28.1 should be presented in the Supplement, and it should be confirmed that it is the only one. In Figure S3, the presence of a neutral density isopycnal 28.2 up to 40°N in the Atlantic looks strange. In reality, this isopycnal inclines to the bottom when crossing abyssal sills near the equator. In the Indian Ocean, the inclination to the bottom begins already at 10°S, and in the Pacific Ocean, at 15°S. The authors can easily verify this using, for example, the WOD23 database. This discrepancy between Fig. S3 and the observational data indicates either a data processing error on the part of the authors or a discrepancy between the reanalysis data and the actual ocean state. In either case, the authors need to address this problem.

Response: Thank you for identifying this issue. We have examined separately the vertical geometry of the three-dimensional GLORYS12 neutral-density field and its agreement with the observationally based WOA23 climatology. The additional checks comprise (1) adjacent-level inversions in the three-dimensional field, (2) the uniqueness and depth distribution of the $\gamma^n = 28.1$ kg m^{-3} surface, and (3) the zonal-mean hydrographic and bottom-density comparisons in Supplementary Figs. S8 – S9. These checks distinguish the occurrence of local inversions from differences in the large-scale extent of the densest water.

2.1 Neutral-density inversions in the three-dimensional GLORYS12 field

We first examined the original three-dimensional neutral-density field prior to zonal averaging. Among 218,683,701 valid adjacent vertical interfaces, we identified 25,381 local neutral-density inversions, corresponding to only 0.0116% of all valid interfaces. Of the 5,162,577 valid water-column profiles, only 0.4858% contain any inversion. Moreover, 98.98% of affected profiles contain only one inverted interface, and 88.55% of all inversions occur at the uppermost valid interface.

Most importantly for the abyssal analysis in this study, only 14 of the 25,381 inversions (0.0552%) occur within the $\gamma^n = 28.1-28.2$ kg m^{-3} density range. These results indicate that neutral-density inversions are extremely rare in the original three-dimensional field and are particularly uncommon within the dense-water range used for the abyssal diapycnal diagnostics.

To document this assessment without interrupting the methodological flow of the main text, we added a new Supplementary Text S1. The first part now reads:

> *"We assessed the geometry of the neutral-density field used for the isopycnal diagnostics by examining the original three-dimensional GLORYS12* γ^n *field before zonal averaging. Vertical model levels were examined sequentially from shallow to deep. For each pair of adjacent valid levels, an inversion was identified when the neutral density at the deeper level was lower than that at the immediately overlying shallower level, i.e.,* $\gamma^n_{deeper} - \gamma^n_{shallower} < 0$ *. No additional numerical tolerance was imposed; any negative adjacent-level difference was counted as an inversion. The same three-dimensional neutral-density field is used for the cross-density diagnostics described in Sect. 2.3 of the main text. Among 218,683,701 valid adjacent vertical interfaces, 25,381 neutral-density inversions were identified, accounting for 0.0116% of the total. Of the 5,162,577 valid water-column profiles, 0.4858% contained at least one inversion. Among the affected profiles, 98.98% contained a single inverted interface, and 88.55% of all inversions occurred at the uppermost valid interface. Within the abyssal density range* $\gamma^n = 28.1–28.2\ kg\ m^{-3}$*, 14 inversions were identified, corresponding to 0.0552% of the 25,381 inversions across the full density range."*

The corresponding sentence added to Sect. 2.3 now reads:

> *"A quality-control assessment of the three-dimensional neutral-density field, including vertical inversions and the uniqueness of the* $\gamma^n = 28.1\ kg\ m^{-3}$ *surface, is provided in Supplementary Text S1."*

We have also revised the Supplementary Fig. S3 caption to emphasize that the plotted contours represent the zonal-mean neutral-density field, rather than individual three-dimensional neutral surfaces. The revised caption now reads:

> *"Figure S3. Zonal-mean neutral density (*γ^n*, kg m*$^{-3}$*) from GLORYS12 in depth–latitude coordinates for the (a) global ocean, (b) Atlantic Ocean, (c) Pacific Ocean, and (d) Indian Ocean. The contours are calculated from the zonal-mean neutral-density field and show the basin-scale mean density structure; they do not trace the connectivity of individual three-dimensional surfaces. Individual surface depths used in the mapped cross-density diagnostics are obtained from the three-dimensional field, as described in Text S1 and illustrated in Fig. S4b."*

2.2 Uniqueness and topography of the $\gamma^n = 28.1\ \mathrm{kg\ m^{-3}}$ surface

We next directly examined the vertical uniqueness of the $\gamma^n = 28.1\ \mathrm{kg\ m^{-3}}$ surface used in the principal diapycnal-velocity analysis. Among the 3,794,293 water-column profiles in which this density surface is present, 3,794,289 contain exactly one vertical crossing, and only four contain multiple crossings. Thus, the $\gamma^n = 28.1\ \mathrm{kg\ m^{-3}}$

surface is uniquely defined in 99.9999% of the profiles in which it occurs and is therefore effectively single-valued over the analyzed domain.

This assessment is also documented in the second part of Supplementary Text S1:

> *"We also examined the vertical uniqueness of the* $\gamma^n = 28.1\ kg\ m^{-3}$ *surface used in the principal diapycnal-velocity analysis. Among the 3,794,293 water-column profiles in which this density surface is present, 3,794,289 contain exactly one vertical crossing and four contain multiple crossings. The* $\gamma^n = 28.1\ kg\ m^{-3}$ *surface therefore has a single vertical intersection in all but four of the profiles in which it occurs. Its spatial depth distribution is shown in Fig. S4b. These checks characterize the vertical density geometry and the uniqueness of the surface intersections used in the cross-density diagnostics."*

Following the reviewer's suggestion, we have further added the global depth distribution of this surface as Supplementary Fig. S4b. Unlike Supplementary Fig. S3, this panel shows the vertical position of the $\gamma^n = 28.1\ \mathrm{kg\ m^{-3}}$ surface directly from the original three-dimensional neutral-density field.

The revised Supplementary Fig. S4 and its caption are shown below:

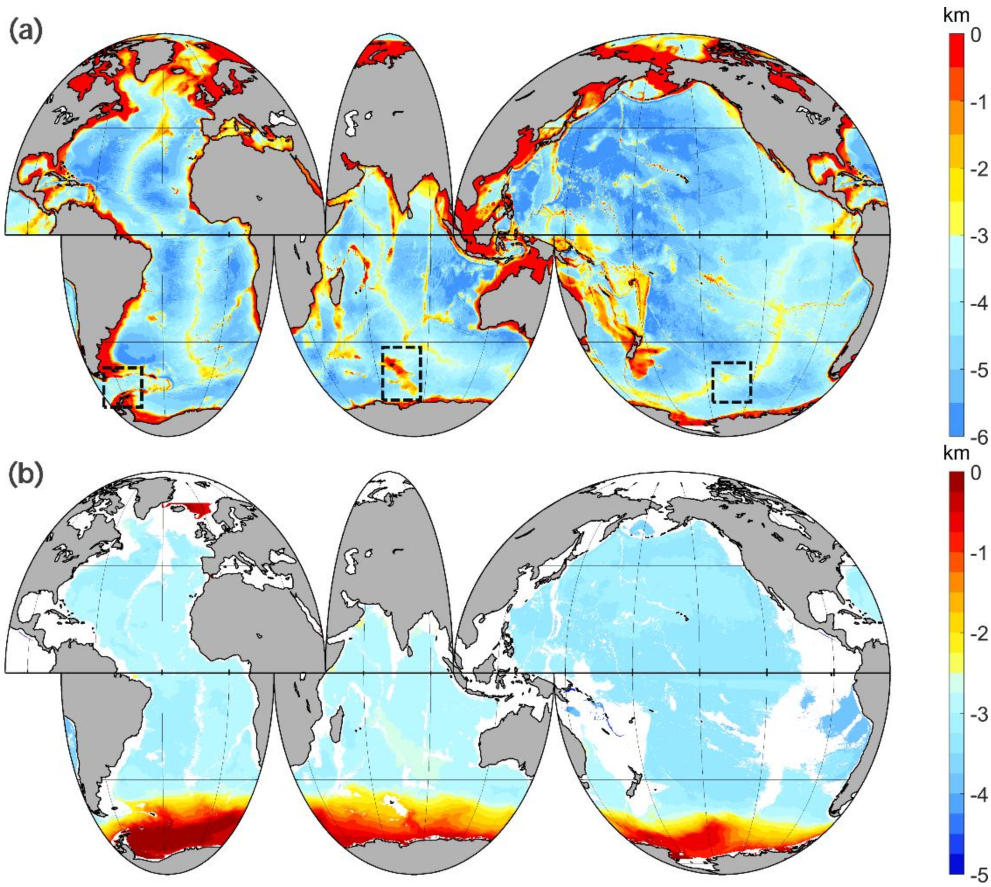

> *"Figure S4. (a) Global bathymetry (km). Black dashed boxes mark the Southern Ocean regions highlighted in Fig. 2a of the main text: Drake*

Passage, the Kerguelen Plateau, and the Pacific–Antarctic Ridge sector near the Udintsev and Eltanin fracture zones. (b) Vertical position (km) of the $\gamma^n = 28.1\ kg\ m^{-3}$ *neutral-density surface diagnosed from the three-dimensional GLORYS12 field. Negative values in both panels indicate positions below sea level. White ocean regions in panel (b) indicate locations where this surface is absent."*

Because Supplementary Fig. S4 now contains two panels, references specifically referring to the global bathymetry elsewhere in the manuscript have also been changed from "Supplementary Fig. S4" to "Supplementary Fig. S4a."

2.3 Comparison of the $\gamma^n = 28.2\ \mathrm{kg\ m^{-3}}$ structure with the observationally based WOA climatology

We calculated neutral density from the WOA23 climatology and constructed corresponding zonal-mean depth–latitude sections for the global ocean and the three major basins (Supplementary Fig. S8). This provides an observationally based comparison for the dense-water geometry questioned by the reviewer.

The comparison shows broadly similar basin-scale stratification but also confirms differences in the extent of the densest contours. In particular, the $\gamma^n = 28.2$ kg m^{-3} contour extends farther north in the GLORYS12 zonal-mean sections than in WOA23 in the Atlantic, Pacific, and Indian Oceans (Supplementary Figs. S3 and S8). We have revised Supplementary Text S1 and the Discussion to describe these differences explicitly in all three basins.

The WOA zonal-mean neutral-density structure is shown in Supplementary Fig. S8 below:

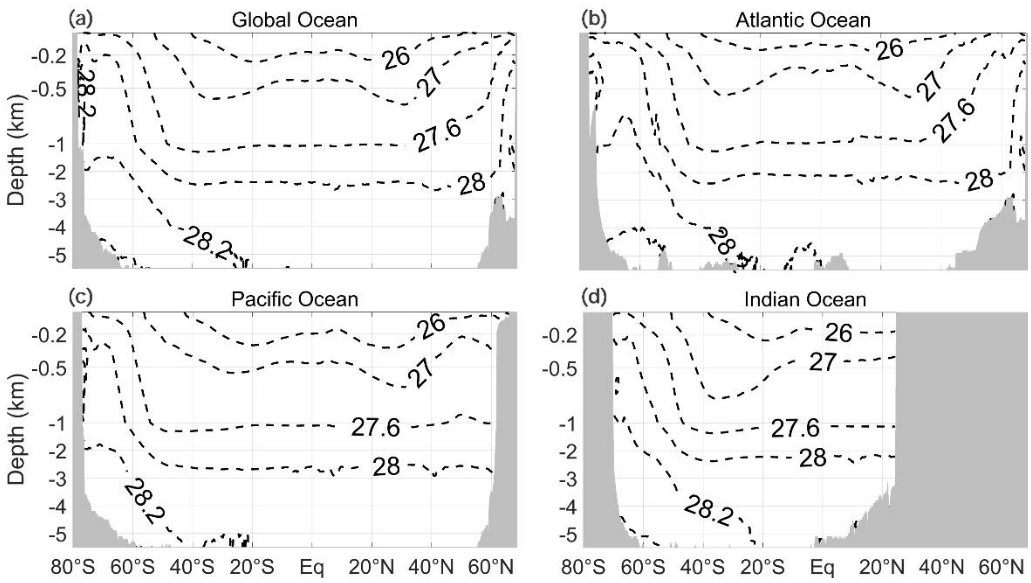

"Figure S8. Zonal-mean neutral density (γ^n, kg m^{-3}) calculated from the World Ocean Atlas 2023 (WOA23) climatology in depth–latitude coordinates for the (a) global ocean, (b) Atlantic Ocean, (c) Pacific Ocean,

and (d) Indian Ocean. The contours provide a hydrographic comparison with the GLORYS12 zonal-mean sections in Fig. S3."

The bottom-density comparison (Supplementary Fig. S9) shows differences near γ^n = 28.2 kg m^{-3} as well as similar large-scale meridional variations. Differences near a fixed density label can change the occurrence and extent of the corresponding surface. Furthermore, the contours in Figs. S3 and S8 are obtained from zonal-mean density fields and do not trace individual connected three-dimensional surfaces. The profile-based checks separately show that widespread vertical inversions do not characterize the GLORYS12 field. We therefore distinguish these geometric checks from the hydrographic differences identified by the WOA23 comparison.

The bottom-density comparison is shown in Supplementary Fig. S9 below:

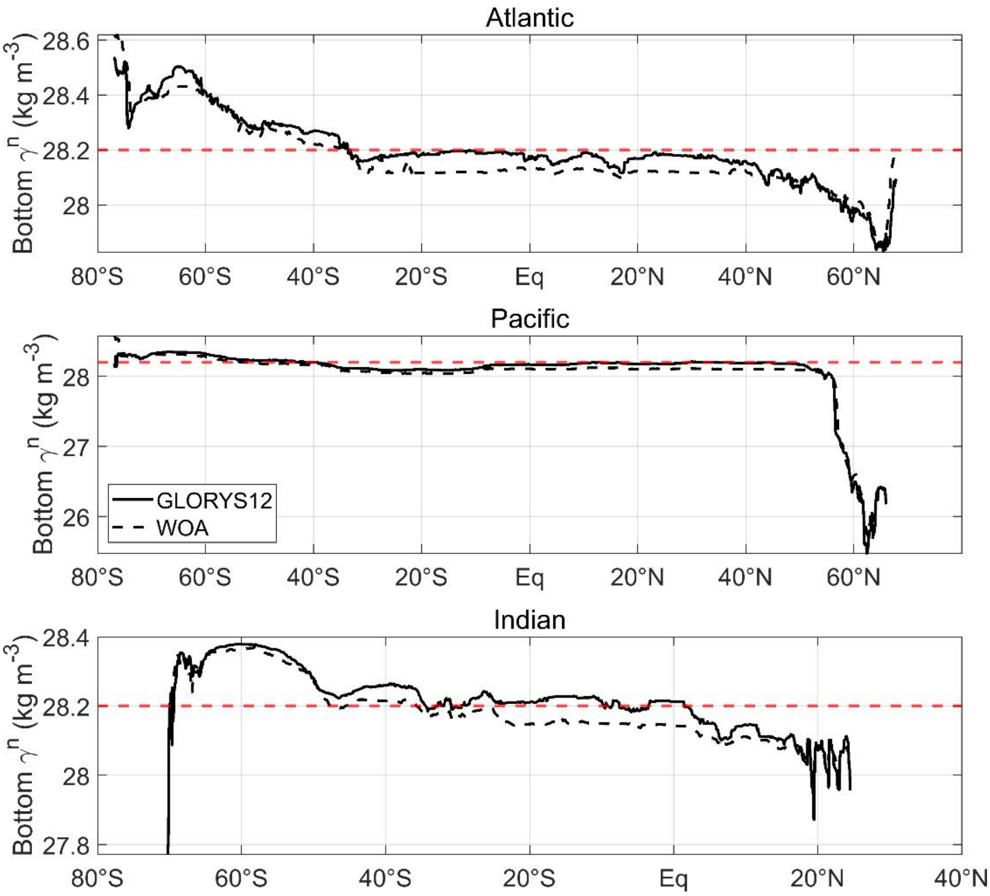

"Figure S9. Zonal-mean bottom neutral density (γ^n, kg m^{-3}) from GLORYS12 (solid black lines) and the World Ocean Atlas 2023 (WOA23) climatology (dashed black lines) in the Atlantic (top), Pacific (middle), and Indian Ocean (bottom). Red dashed lines mark γ^n=28.2 kg m^{-3}. The vertical scales differ among panels."

The revised Discussion relates these findings to the scope of the transport interpretation:

"Because the present analysis relies on a single ocean reanalysis, regional structures and transport magnitudes remain subject to product-dependent

uncertainty. Local neutral-density inversions are rare in the three-dimensional GLORYS12 field, and the $\gamma^n = 28.1\ kg\ m^{-3}$ *surface used for the principal mapped diagnostics is effectively single-valued (Supplementary Text S1 and Fig. S4b). The comparison with the observationally based World Ocean Atlas 2023 (WOA23) climatology shows broadly similar basin-scale stratification, but the* $\gamma^n = 28.2\ kg\ m^{-3}$ *contour has a more southerly extent in the WOA23 zonal-mean sections of the Atlantic, Pacific, and Indian Oceans (Supplementary Figs. S3 and S8). Differences in bottom density near this label (Supplementary Fig. S9) can alter the occurrence and available area of a fixed density surface. The inversion and uniqueness checks establish the local geometry used for the diagnostics, while the hydrographic comparison identifies differences in the represented dense-water structure. The regional transport magnitudes and their density dependence are therefore interpreted within the GLORYS12 framework. Within this framework, the Southern Ocean's leading regional contribution is evident across a range of density surfaces (Supplementary Fig. S5) and is supported by the concentration and ventilation-thickness patterns (Figs. 3 and 4). These complementary diagnostics support the regional interpretation without establishing that the exact transport magnitudes are independent of the hydrographic product."*

Together, these checks address the inversion concern and document the topography and near-uniqueness of the $\gamma^n = 28.1\ kg\ m^{-3}$ surface used in the principal mapped diagnostics. The WOA23 comparison also identifies differences in the dense-water extent, which we now describe explicitly. Accordingly, we retain the basin comparison as a diagnosis within GLORYS12 and qualify the precise regional transports and their density dependence. The Southern Ocean interpretation draws on the regional transport curves across multiple density surfaces and the tracer distributions, rather than on the apparent northern termination of a single zonal-mean contour.

3. Lines 102-103. The system of partial differential equations is incomplete; it lacks initial/boundary conditions. For example, the initial C and Γ distributions are not specified. What 100 years are we talking about? Is this a forecast or a solution under stationary boundary conditions that simulate only seasonal variations?

Response: Thank you for this important comment. We agree that the original description of the CART experiment did not explicitly specify the initial and source conditions for the concentration and age concentration. We have therefore clarified how the bottom-water tracer is initialized and continuously supplied during the integration.

Specifically, the concentration is initialized to C=1 in the model bottom layer and C=0 in the ocean interior, while the initial age concentration is set to Γ=0 throughout the domain. During the integration, the model bottom layer is continuously restored to C=1, so that newly introduced bottom-water tracer enters the experiment with zero age. This source-layer treatment is consistent with the CART formulation in which the age of newly introduced tracer is reset to zero at the source.

We have also clarified the meaning of the 100-year integration. The experiment is not a forecast over 100 calendar years. Instead, the CART equations are integrated for 100 model years under the prescribed monthly climatological forcing, with the climatological annual cycle repeated throughout the integration. The 100-year period therefore represents the finite integration window used to diagnose the evolution and renewal of bottom-water influence.

The revised text now reads:

> *"To represent bottom-water-origin ventilation, the concentration is initialized as*
>
> $$C(x,0) = \begin{cases} 1, & x \in \Omega_b \\ 0, & x \in \Omega_i \end{cases} \qquad (4)$$
>
> *where Ω_b denotes the model bottom layer and Ω_i denotes the ocean interior. The initial age concentration is set to $\Gamma(x,0) = 0$ throughout the domain. During the integration, the model bottom layer is continuously restored to C=1:*
>
> $$C(x,t) = 1, \quad x \in \Omega_b, \quad t > 0, \qquad (5)$$
>
> *This prescription provides a continuous source of newly introduced bottom-water tracer, with zero age assigned at the source layer.*
>
> *Using these initial and source-layer conditions, the CART equations are integrated continuously for 100 years under the monthly climatological forcing derived from GLORYS12. Here, the 100-year period denotes the model integration time under the climatological forcing rather than 100 calendar years of transient ocean evolution. The diagnosed ages measure elapsed time for the tagged component under the repeated climatological annual cycle."*

Technical corrections

1. *Line 89. Add the abbreviation CART to subheading 2.1.*

Response: Thank you for this suggestion. We have added the abbreviation "CART" to the subsection heading as suggested. The revised heading now reads:

> ***"2.1 Constituent-oriented Age and Residence time Theory (CART)"***

2. *Captions to Figure 2 and throughout the text and in the Supplementary Appendix: The highlighted framework in the Pacific Ocean is not the Campbell Plateau, but a section of the mid-ocean ridge at its intersection with the Udintsev and Eltanin fracture zones. The Campbell Plateau is located south of New Zealand and is the shelf of its microcontinent.*

Response: Thank you for pointing this out. We agree that the Pacific-sector region highlighted in Fig. 2a was incorrectly identified as the Campbell Plateau. After rechecking the bathymetry and published descriptions of the central South Pacific topography, we find that this region corresponds to the Pacific–Antarctic Ridge sector near the Udintsev and Eltanin fracture zones. We have therefore corrected this geographic identification throughout the manuscript and Supplementary Materials.

The corrected identification is also consistent with previous studies of Southern Ocean topographic upwelling. Tamsitt et al. (2017) and Yung et al. (2022) identified Drake Passage, the Kerguelen Plateau, and the Pacific–Antarctic Ridge among the major topographic hotspots of Southern Ocean upwelling, while Park et al. (2019) described the relationship of the Udintsev and Eltanin fracture zones to the Pacific–Antarctic Ridge system in the central South Pacific.

The relevant part of the revised Fig. 2 caption now reads:

> *"Black dashed boxes mark representative Southern Ocean hotspots of intensified diapycnal upwelling associated with major topographic features, including Drake Passage, the Kerguelen Plateau, and the Pacific–Antarctic Ridge sector near the Udintsev and Eltanin fracture zones."*

The corresponding Results text now reads:

> *"In the Southern Ocean, enhanced upward motion is evident near major topographic regions, including Drake Passage, the Kerguelen Plateau, and the Pacific–Antarctic Ridge sector near the Udintsev and Eltanin fracture zones (Park et al., 2019), as highlighted in Fig. 2a and Supplementary Fig. S4a. These regions correspond to major topographic upwelling hotspots identified in previous high-resolution studies (Tamsitt et al., 2017; Yung et al., 2022)."*

We have also corrected the corresponding geographic identification in the discussion of Fig. 5. The revised text now reads:

> *"In the Southern Ocean, the strongest upward fluxes align with Drake Passage, the Kerguelen Plateau, and the Pacific–Antarctic Ridge sector near the Udintsev and Eltanin fracture zones, reinforcing the inference that rough topography and associated mixing hotspots organize a substantial fraction of abyssal return (Baker et al., 2023; Ferrari, 2014; Ferrari et al., 2016; Ledwell et al., 2000; Wynne-Cattanach et al., 2024)."*

The revised Supplementary Fig. S4 caption now reads:

> *"Figure S4. (a) Global bathymetry (km). Black dashed boxes mark the Southern Ocean regions highlighted in Fig. 2a of the main text: Drake Passage, the Kerguelen Plateau, and the Pacific–Antarctic Ridge sector near the Udintsev and Eltanin fracture zones."*

3. *Line 147. The reference to Marshall et al. 1999 is incorrect. Potential density was used in that work. Please reformulate the link.*

Response: Thank you for pointing this out. We agree that our original wording was not sufficiently precise because Marshall et al. (1999) formulated the moving-density-surface framework using potential density, whereas neutral density γ^n is used in the present study. Our calculation follows the same general kinematic framework for flow relative to a moving density surface, but applies it to the neutral-density field. The use of moving neutral-density surfaces for diagnosing cross-density motion is consistent with subsequent neutral-density formulations, including Iudicone et al. (2008) and Lang et al. (2020). We have therefore revised the attribution to distinguish the original potential-density formulation from our neutral-density implementation.

The corresponding text now reads:

"$\boldsymbol{n}_\rho = \nabla\gamma^n/|\nabla\gamma^n|$ is the unit normal vector to the isopycnal surface, and γ^n is the neutral density from GLORYS12. The neutral density was calculated from salinity, temperature, and pressure using the neutral-density algorithm of Jackett and McDougall (1997), which labels hydrographic profiles relative to a globally referenced neutral-density field. Following the general kinematic framework for flow relative to moving density surfaces (Marshall et al., 1999; Ferrari et al., 2016), we apply this formulation to the neutral-density field. The velocity of the moving neutral-density surface, $\boldsymbol{u}_\rho$, is therefore given by

$$\boldsymbol{u}_\rho = -\frac{1}{|\nabla\gamma^n|}\frac{\partial\gamma^n}{\partial t}\boldsymbol{n}_\rho, \qquad (8)$$

For the signed diapycnal-velocity diagnostics used below, we use the scalar normal component $\omega_d = \boldsymbol{\omega}_d \cdot \boldsymbol{n}_\rho$, rather than the vector $\boldsymbol{\omega}_d$ itself. Because $\boldsymbol{n}_\rho$ points toward increasing γ^n, positive values denote motion toward denser neutral-density classes, whereas negative values denote motion toward lighter classes.

The use of neutral-density surfaces for diagnosing cross-density motion follows the neutral-density framework developed in subsequent studies (Iudicone et al., 2008; Lang et al., 2020)."

4. *Line 184. Hotspots in Figure 2a are located not only in the equatorial Pacific, but also in the Indian and Atlantic Oceans.*

Response: Thank you for pointing this out. We agree that the equatorial upwelling hotspots in Fig. 2a are not limited to the Pacific Ocean, but are also evident in the Indian and Atlantic Oceans. We have revised the corresponding description accordingly. The revised text now reads:

> *"The most prominent upwelling hotspots occur in the Southern Ocean, across equatorial regions of the Pacific, Indian, and Atlantic Oceans, and in selected deep western boundary regions."*

5. *Line 191. Since the authors are simulating seasonal variation, the question arises: to what averaging period does Figure 2a refer? For which 30 years out of 100 were the averaging performed to construct Figures 2b-e?*

Response: Thank you for raising this point. The diapycnal-velocity diagnosis shown in Fig. 2 is independent of the 100-year CART integration. Both the CART experiment and the diapycnal-velocity diagnosis use monthly climatological fields constructed from the GLORYS12 reanalysis over 1994–2022.

To make this distinction explicit, we have added the description of the GLORYS12 climatology in the revised manuscript:

> *"For this study, monthly climatological temperature, salinity, and velocity fields were constructed from the GLORYS12 reanalysis over the period 1994–2022. These climatological fields were then used as the input for the CART experiment and for the diapycnal-velocity diagnosis described below."*

Figure 2a therefore shows the annual-mean diapycnal velocity diagnosed directly from the 1994–2022 GLORYS12 monthly climatology, and Figs. 2b–e show the corresponding zonal-mean annual climatological fields. Thus, the "30-year mean" in the original manuscript did not refer to any selected 30-year period within the 100-year CART integration. We have removed this wording and clarified the temporal basis of the diapycnal-velocity diagnostics.

Accordingly, the revised Fig. 2 caption now reads:

> *"Figure 2 Diapycnal velocity ($m\,s^{-1}$) as a diagnostic of global ocean diapycnal motion. (a) Global distribution of annual-mean diapycnal velocity diagnosed from the 1994–2022 GLORYS12 climatological fields on the neutral-density surface $\gamma^n = 28.1\ kg\,m^{-3}$ … (b–e) Zonal-mean distributions of annual-mean diapycnal velocity diagnosed from the 1994–2022 GLORYS12 climatological fields in the global ocean, Atlantic Ocean, Pacific Ocean, and Indian Ocean. Together, these panels illustrate the large-scale spatial organization of cross-isopycnal exchange in the global overturning circulation."*

We also revised the corresponding text now reads:

> *"Having established the horizontal localization of abyssal diapycnal exchange, we next examine its large-scale vertical and basin-scale*

organization using the zonal-mean climatological diapycnal velocity fields shown in Fig. 2b–e."

For clarity, the 100-year period mentioned elsewhere in the manuscript refers only to the CART diagnostic integration under repeated monthly climatological forcing. These 100 years are integration years rather than calendar years, and the CART results are analyzed using annual-mean outputs.

6. *To what averaging period does Figure 4 refer?*

Response: Thank you for this helpful question. Figure 4 does not represent an average over a selected period of the 100-year CART integration. In the CART experiment, annual-mean concentration and water-age fields were obtained for each integration year. At each location, once the bottom-water signal arrives, the concentration initially increases rapidly, after which its rate of increase gradually decreases as the concentration approaches a quasi-equilibrium state. We therefore use the temporal tendency of concentration ($\partial C/\partial t < 10^{-3}$ yr^{-1}) to diagnose the local quasi-equilibrium time.

To clarify this procedure, we revised the corresponding description in Sect. 2.1. The revised text now reads:

"Using these initial and source-layer conditions, the CART equations are integrated continuously for 100 years under the monthly climatological forcing derived from GLORYS12. Here, the 100-year period denotes the model integration time under the climatological forcing rather than 100 calendar years of transient ocean evolution. The diagnosed ages measure elapsed time for the tagged component under the repeated climatological annual cycle. Water age is diagnosed as $A = \Gamma/C$ only where $C > 0$. At locations where $C = 0$, or where the resulting age value is numerically invalid, A is assigned NaN and excluded from subsequent diagnostics.

Annual-mean concentration and water-age fields were obtained for each integration year. At each location, once the bottom-water signal arrives, the concentration initially increases rapidly, after which its rate of increase gradually decreases as the concentration approaches a quasi-equilibrium state. We therefore identify the local quasi-equilibrium time as the first post-arrival integration year at which the concentration tendency ($\partial C/\partial t$) falls below $10^{-3}\ yr^{-1}$. The annual-mean concentration and corresponding water age are sampled at this locally diagnosed time for subsequent analysis, so sampling times can differ among locations. For locations that do not satisfy this criterion within the 100-year integration, the diagnostic sampling time is set to integration year 100; these locations are regarded as not having reached quasi-equilibrium within the present integration window."

Accordingly, the concentration field shown in Fig. 4 is based on the annual-mean concentration corresponding to the locally diagnosed quasi-equilibrium time, rather than on a temporal average over a prescribed subset of the 100-year integration.

Following this clarification, we also revised the corresponding text now reads:

> *"Using concentration sampled at the local diagnostic times defined in Sect. 2.1, we next examine the basin-scale distribution of bottom-water influence in density space (Fig. 4). The zonal-mean concentration fields provide a basin-comparative view of bottom-water return pathways."*

The Fig. 4 caption has also been revised to specify the local diagnostic sampling times:

> *"Figure 4 Zonal-mean distributions of bottom-water tracer concentration sampled at the local diagnostic times defined in Sect. 2.1 in the (a) global ocean, (b) Atlantic Ocean, (c) Pacific Ocean, and (d) Indian Ocean."*

7. *In Figure 5a and its caption, the transport cannot be in Sv; it must be expressed per unit area. In Figure 5b, the transport can be expressed in Sv, but then it is necessary to indicate which density step it refers to. Otherwise, the transport must be expressed in transport/density units.*

Response: Thank you for pointing this out. We agree that the units and definitions of the quantities shown in Fig. 5a and Fig. 5b were not sufficiently clear in the original manuscript. The quantity shown in Fig. 5a has already been multiplied by the horizontal area (dxdy) of each grid cell and therefore represents the local grid-cell contribution to the concentration-weighted diapycnal transport, rather than a transport integrated over the entire density surface. We have accordingly revised its unit from Sv to Sv grid cell^{-1}.

For Fig. 5b, the grid-cell transports are integrated separately on neutral-density surfaces spaced at intervals of $0.1\ \mathrm{kg\ m^{-3}}$. We have now explicitly specified this surface spacing in the figure caption. The corresponding Results text has also been adjusted to distinguish the local grid-cell transport in Fig. 5a from the integrated transport evaluated across successive neutral-density surfaces in Fig. 5b.

The revised Fig. 5 caption now reads:

> *"Figure 5 Concentration-weighted diapycnal transport and the coupling between diapycnal motion and bottom-water concentration. (a) Global distribution of grid-cell concentration-weighted diapycnal transport (Sv grid cell-1) on the neutral-density surface $\gamma^n = 28.1\ kg\ m^{-3}$. Positive values indicate transport toward denser classes (downwelling), whereas negative values indicate transport toward lighter classes (upwelling). Black dashed boxes mark representative Southern Ocean hotspots of intensified upward transformation. (b) Integrated concentration-weighted diapycnal transport (Sv) evaluated separately on neutral-density surfaces spaced at intervals of $0.1\ kg\ m^{-3}$, including upwelling transport (green), downwelling transport (yellow), and net transport (black)."*

The corresponding Results text now reads:

> *"Strong local upward concentration-weighted diapycnal transports in Fig. 5a are concentrated in the Southern Ocean, the equatorial Pacific, and parts of the equatorial Atlantic."*

and

> *"The integrated transport evaluated across successive neutral-density surfaces (Fig. 5b) further clarifies where this transformation is concentrated."*

8. *Line 395. «This old-age structure is consistent with the basin's strong stratification and comparatively weak deep overturning, which limit upward renewal once bottom waters leave the Southern Ocean source sectors.» This sentence is unclear, since the abyssal and deep density stratification of the Pacific Ocean north of the ACC band is weakest compared to the Indian and Atlantic Oceans. And weakening stratification should facilitate overturning.*

Response: Thank you for pointing this out. We agree that our original reference to "strong stratification" in the Pacific was not appropriate. In particular, the deep and abyssal Pacific north of the ACC is not characterized by stronger stratification than the Atlantic and Indian Oceans, and stratification alone cannot explain the relatively old bottom-water ages diagnosed in this basin. Our intention was to emphasize the comparatively slow renewal of bottom-water influence in the Pacific. We have therefore removed the reference to strong stratification and revised the text to relate the old-age structure more directly to the long basin-scale transport pathways, the absence of strong northern deep-water formation, and the relatively limited upward transformation of bottom-water influence diagnosed in our results. The revised text now reads:

> *"This old-age structure is consistent with the comparatively slow renewal of bottom-water influence in the Pacific, where long basin-scale transport pathways, the absence of strong northern deep-water formation, and limited upward penetration contribute to prolonged renewal times away from the Southern Ocean source sectors (Talley, 2013; Tamsitt et al., 2017)."*

9. *Line 452. What is "first-order asymmetry"? Restate or expand on the concept.*

Response: Thank you for pointing this out. We agree that the term "first-order asymmetry" was too vague. Here, we intended to refer to the basin-scale differences in bottom-water return consistently identified by the complementary diagnostics, including Southern Ocean dominance, comparatively strong upward penetration in the Atlantic, slower renewal in the Pacific, and more localized return pathways in the Indian Ocean. We have therefore replaced the original wording with a more explicit description. The revised text now reads:

> *"The concentration and age fields reveal related spatial contrasts: the Southern Ocean dominates the large-scale return of bottom-water influence,*

the Atlantic supports the strongest upward penetration but with substantial northward aging, the Pacific shows older bottom-water signals together with comparatively limited upward penetration, and the Indian Ocean contains more localized return corridors."

References cited in this response

Baker, L. E., Mashayek, A., and Naveira Garabato, A. C.: Boundary Upwelling of Antarctic Bottom Water by Topographic Turbulence, AGU Adv., 4, e2022AV000858, https://doi.org/10.1029/2022AV000858, 2023.

Broecker, W. S., Peacock, S. L., Walker, S., Weiss, R., Fahrbach, E., Schroeder, M., Mikolajewicz, U., Heinze, C., Key, R., Peng, T.-H., and Rubin, S.: How much deep water is formed in the Southern Ocean?, J. Geophys. Res.-Oceans, 103, 15833–15843, https://doi.org/10.1029/98JC00248, 1998.

De Lavergne, C., Madec, G., Le Sommer, J., Nurser, A. J. G., and Naveira Garabato, A. C.: On the Consumption of Antarctic Bottom Water in the Abyssal Ocean, J. Phys. Oceanogr., 46, 635–661, https://doi.org/10.1175/JPO-D-14-0201.1, 2016.

Ferrari, R.: What goes down must come up, Nature, 513, 179–180, https://doi.org/10.1038/513179a, 2014.

Ferrari, R., Mashayek, A., McDougall, T. J., Nikurashin, M., and Campin, J.-M.: Turning Ocean Mixing Upside Down, J. Phys. Oceanogr., 46, 2239–2261, https://doi.org/10.1175/JPO-D-15-0244.1, 2016.

Ganachaud, A.: Large-scale mass transports, water mass formation, and diffusivities estimated from World Ocean Circulation Experiment (WOCE) hydrographic data, J. Geophys. Res.-Oceans, 108, 3213, https://doi.org/10.1029/2002JC001565, 2003.

Iudicone, D., Madec, G., and McDougall, T. J.: Water-Mass Transformations in a Neutral Density Framework and the Key Role of Light Penetration, J. Phys. Oceanogr., 38, 1357–1376, https://doi.org/10.1175/2007JPO3464.1, 2008.

Jackett, D. R. and McDougall, T. J.: A Neutral Density Variable for the World's Oceans, Journal of Physical Oceanography, 27, 237–263, https://doi.org/10.1175/1520-0485(1997)027<0237:ANDVFT>2.0.CO;2, 1997.Lang, Y., Stanley, G. J., McDougall, T. J., and Barker, P. M.: A Pressure-Invariant Neutral Density Variable for the World's Oceans, J. Phys. Oceanogr., 50, 3585–3604, https://doi.org/10.1175/JPO-D-19-0321.1, 2020.

Ledwell, J. R., Montgomery, E. T., Polzin, K. L., St. Laurent, L. C., Schmitt, R. W., and Toole, J. M.: Evidence for enhanced mixing over rough topography in the abyssal ocean, Nature, 403, 179–182, https://doi.org/10.1038/35003164, 2000.

Marshall, J., Jamous, D., and Nilsson, J.: Reconciling thermodynamic and dynamic methods of computation of water-mass transformation rates, Deep-Sea Res. Pt. I, 46, 545–572, https://doi.org/10.1016/S0967-0637(98)00082-X, 1999.

Orsi, A. H., Smethie, W. M., and Bullister, J. L.: On the total input of Antarctic waters to the deep ocean: A preliminary estimate from chlorofluorocarbon measurements, J. Geophys. Res.-Oceans, 107, 3122, https://doi.org/10.1029/2001JC000976, 2002.

Park, Y.-H., Park, T., Kim, T.-W., Lee, S.-H., Hong, C.-S., Lee, J.-H., Rio, M.-H., Pujol, M.-I., Ballarotta, M., Durand, I., and Provost, C.: Observations of the Antarctic Circumpolar Current Over the Udintsev Fracture Zone, the Narrowest Choke Point in the Southern Ocean, J. Geophys. Res.-Oceans, 124, 4511–4528, https://doi.org/10.1029/2019JC015024, 2019.

Peacock, S., Visbeck, M., and Broecker, W.: Deep Water Formation Rates Inferred from Global Tracer Distributions: An Inverse Approach, in: Inverse Methods in Global Biogeochemical Cycles, Geophys. Monogr. Ser., 114, 185–195, https://doi.org/10.1029/GM114p0185, 2000.

Talley, L.: Closure of the Global Overturning Circulation Through the Indian, Pacific, and Southern Oceans: Schematics and Transports, Oceanography, 26, 80–97, https://doi.org/10.5670/oceanog.2013.07, 2013.

Tamsitt, V., Drake, H. F., Morrison, A. K., Talley, L. D., Dufour, C. O., Gray, A. R., Griffies, S. M., Mazloff, M. R., Sarmiento, J. L., Wang, J., and Weijer, W.: Spiraling pathways of global deep waters to the surface of the Southern Ocean, Nat. Commun., 8, 172, https://doi.org/10.1038/s41467-017-00197-0, 2017.

Tamsitt, V., Abernathey, R. P., Mazloff, M. R., Wang, J., and Talley, L. D.: Transformation of Deep Water Masses Along Lagrangian Upwelling Pathways in the Southern Ocean, J. Geophys. Res.-Oceans, 123, 1994–2017, https://doi.org/10.1002/2017JC013409, 2018.

Wynne-Cattanach, B. L., Couto, N., Drake, H. F., Ferrari, R., Le Boyer, A., Mercier, H., Messias, M.-J., Ruan, X., Spingys, C. P., Van Haren, H., Voet, G., Polzin, K., Naveira Garabato, A. C., and Alford, M. H.: Observations of diapycnal upwelling within a sloping submarine canyon, Nature, 630, 884–890, https://doi.org/10.1038/s41586-024-07411-2, 2024.

Yung, C. K., Morrison, A. K., and Hogg, A. McC.: Topographic Hotspots of Southern Ocean Eddy Upwelling, Front. Mar. Sci., 9, 855785, https://doi.org/10.3389/fmars.2022.855785, 2022.